A Low-Density M-type Asteroid in the Main Belt

J. L. Margot* and M. E. Brown

The orbital parameters of a satellite revolving around 22 Kalliope indicate that the bulk density of this main-belt asteroid is 2.37 ± 0.4 grams per cubic centimeter. M-type asteroids such as Kalliope are thought to be the disrupted metallic cores of differentiated bodies. The low density indicates that Kalliope cannot be predominantly composed of metal and may be composed of chondritic material with ~30% porosity. The satellite orbit is circular, suggesting that Kalliope and its satellite have different internal structures and tidal dissipation rates. The satellite may be an aggregate of impact ejecta from an earlier collision with Kalliope.

The main belt of asteroids between Mars and Jupiter is known to exhibit a strong compositional gradient as a function of heliocentric distance (*1*). This zoning represents an important constraint on the formation conditions (temperature, pressure, and chemistry) of planetesimals in the primordial solar nebula. Asteroids also preserve the signature of processes that affect the formation of solid planets, including accretion, chemical and thermal alteration, and differentiation. Understanding the compositional structure and heating history of the asteroids in the main belt provides valuable clues to the formation history of the solar system.

Asteroids are classified into types on the basis of their visible and near-infrared reflectance properties (*2*). Surface compositions can be inferred from those properties, but the mineralogical interpretation of the various spectral types is not unique. The M-type class of asteroids are characterized by a moderate albedo (~10 to 25%), a flat or slightly red spectral curve, and the general lack of absorption features (*3*). The spectra of M-type asteroids are consistent with metallic iron-nickel; hence, they have been traditionally interpreted as the parent bodies of iron meteorites. However, a combination of spectrally neutral silicates such as enstatite ($MgSiO_3$) and metal grains yield similar spectra (*4*, *5*), such that enstatite chondrite meteorites are also plausible analogs. Here we examined the dynamic properties of the M-type asteroid Kalliope and its recently discovered satellite (*6*) to determine the density and infer the composition of Kalliope (*7*).

22 Kalliope is a ~181-km-diameter asteroid that was discovered on 16 November 1852 by J. R. Hind. The existence of its satellite was unknown until observations at the W. M. Keck II telescope on Mauna Kea, Hawaii, on 29 August 2001 (*6*, *8*). Our observations were made with the adaptive optics system (*9*), which relies on a Shack-Hartmann wavefront sensor sensitive to visible light and a 349-element deformable mirror that corrects the infrared light reaching the science instruments. We observed at 1.6-μm wavelength with SCAM, a 256 × 256 HgCdTe detector that is part of the NIRSPEC instrument (*10*). In a typical observing run, we record a 5- to 10-s test exposure to determine the desired integration time, ensuring that the detector does not saturate. We then nod the telescope to four different offset positions and take an exposure with the science target centered in each one of four quadrants. This procedure allows for sky subtraction and minimizes the impact of detector defects. For Kalliope we used six subexposures of 10 s each, resulting in a total integration time of 1 min for each one of the quadrants.

The satellite was seen in the 10-s test exposure at 2001-08-29 14:44 UTC. Immediate confirmation was obtained during the normal sequence of 1-min exposures. The discovery image of the companion to Kalliope is shown in Fig. 1A. Because the telescope tracks at a nonsidereal rate, it is unlikely that a background object would maintain a constant relative position with respect to the primary over the course of several minutes. We obtained additional confirming observations on 31 August and 1 September.

We estimated the size of the satellite by measuring the primary to secondary photon flux ratio. We carefully removed an azimuthally averaged profile of the primary before obtaining flux measurements for the secondary. We find an average flux ratio of 25 ± 5 (a magnitude difference of 3.5) using images obtained at multiple epochs and with multiple detectors. The error bars represent the spread in the measurements and not the actual uncertainty, which could be much larger owing to the difficulty in separating the flux from the two components. The primary is resolved and its shape is unknown, such that deconvolution with the variable point-spread function of the adaptive optics system is not practical. Assuming that both components have similar albedos, the ratio of radii is therefore $R_p/R_s \cong 5$ (within a factor of 2), where subscripts *p* and *s* refer to primary and secondary, respectively. If both components have the same bulk density, the mass ratio $M_p/M_s \cong 125$.

The position of the secondary with respect to the primary was measured on several nights over the past few months (Table 1). The angular separation and position angle (measured positive east of north) were esti-

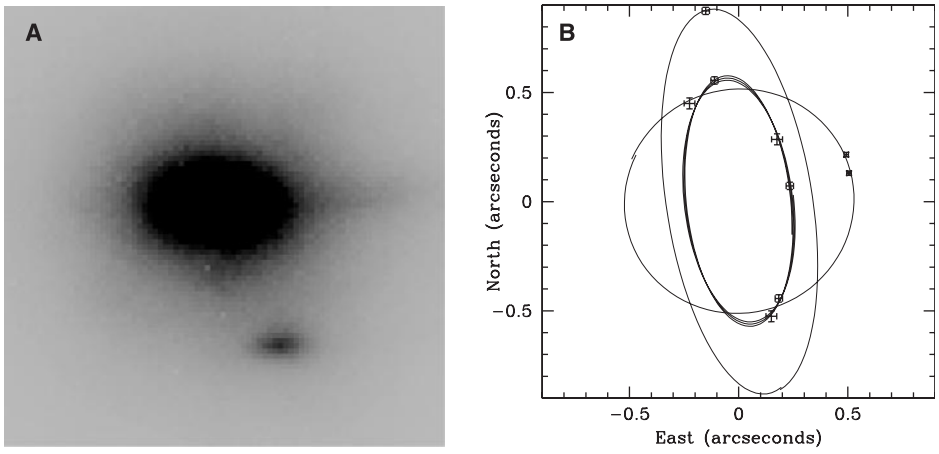

Fig. 1. (**A**) Discovery image of the companion to 22 Kalliope obtained at the W. M. Keck II telescope on 29 August 2001. [The corresponding modified Julian date (MJD) is 52150.] The image has been rotated and scaled to approximately match the figure at right. (**B**) The apparent orbit of the companion about the primary at the epochs of our observations. Astrometric positions of the secondary with respect to the primary (origin) and their error bars are shown as symbols. The solid lines represent three revolutions at epochs MJD 52150 to 52161, one revolution at epoch MJD 52253, and one revolution at epoch MJD 52637. Large variations in the apparent orbit are seen because of considerable distance and aspect changes during the ~500-day span.

Division of Geological and Planetary Sciences, California Institute of Technology, Pasadena, CA 91125, USA.

*To whom correspondence should be addressed. E-mail: margot@gps.caltech.edu

mated by differencing the positions of the centroids of the primary and secondary. Removal of a best-guess model for the wings of the point-spread function did not affect the astrometry appreciably. In addition to the SCAM detector described above, we used the NIRC2 detector on Keck II and the PHARO camera (*11*) at the 200-inch telescope in Palomar, California. Plate scales for those instruments are 17, 25, and 10 milliarc sec/pixel, respectively, and are known to ~1% accuracy. We assigned positional uncertainties to our measurements equivalent to the plate scale.

The program developed for fitting orbits to range-Doppler observations of binary near-Earth asteroids (*12*) was extended to handle the case of optical observations. This program solves the two-body problem and takes account of aspect variations due to geocentric distance variations and motion of the asteroid across the sky. Corrections are also applied for light travel time (*13*).

We initially modeled the dynamics of the system with seven parameters: orbital period P, semi-major axis a, eccentricity e, three Euler angles defining the orientation of the orbital plane and the pericenter location (Ω, i, ω), and the epoch of pericenter passage T. All solutions compatible with the data yielded $e \leq 0.015$ with error bars of the same order, indicating that the orbit might be circular. Indeed, an analysis of variance showed that five-parameter models (P, a, Ω, i, T) representing circular orbits fit the data equally well. Because the data do not conflict with the hypothesis $e = 0$, a circular orbit is used in the rest of this paper. As seen by an observer on Earth, the shape of the orbit is an ellipse that varies with time (Fig. 1B).

The best-fit P and a (Table 2) yield a total mass for this system of $M = 7.36 \times 10^{18}$ kg. Assuming for now a perfect knowledge of the mass of the primary, neglecting the <1% mass contribution due to the secondary, and using the IRAS diameter value of 181 km [with 5% uncertainties; i.e., twice the error bars reported by Tedesco *et al.* (*14*)], we obtain a density for the primary of 2.37 ± 0.4 g cm^{-3}. In the next sections, we place error bars on P, a, and M by examining the dynamical aspects of the Kalliope binary system. Analysis of the dynamics also allows us to propose a likely formation mechanism for the binary and to place constraints on asteroid internal structure and mechanical properties. We return to the significance of the low-density measurement at the end of the paper.

The best-fit orbital plane orientation in J2000 equatorial coordinates is at right ascension and declination (RA, DEC) of (196.2°, −3.4°), which corresponds to ecliptic longitude and latitude of (196.2°, +3.2°). It is interesting to compare this orientation with possible orientations of the primary spin vector, which have been derived on the basis of lightcurve observations. In a synthesis, Magnusson *et al.* (*15*) rejected prograde solutions (i.e., spin vector pointing north of the ecliptic) and maintained two retrograde solutions at B1950 ecliptic coordinates (21°, −23°) and (191°, −2°). The former is separated from our orbit pole by 160° whereas the latter is within 7° of our orbit pole. In an earlier work, Magnusson (*16*) indicated a preference for the second spin solution and gave error bars of (±3°, ±5°). Therefore the preferred lightcurve-derived spin pole and our orbital pole are consistent. We argue below that on the basis of tidal evolution scenarios, the angular separation between spin and orbital poles is probably near zero.

So far we have assumed that the orbital plane maintains a constant orientation in inertial space. This may not be valid if there is nonnegligible orbital precession due to the oblateness of the primary. The orbit of a secondary around an oblate primary experiences a regression of the line of nodes at a rate (*17*)

$$\frac{d\Omega}{dt} \cong -\frac{3}{2} n J_2 \left(\frac{R}{a}\right)^2 \qquad (1)$$

where n is the mean motion, J_2 is the second degree coefficient in the spherical harmonic expansion of the gravitational potential, and R is the mean radius of the primary. Based on a triaxial ellipsoid approximation of the primary (*15*) with axis ratios $a/b = 1.32$, $b/c = 1.20$, and the assumption of homogeneous density, we infer $J_2 \cong 0.12$ and a precession period on the order of 8 years. However, because of the near coincidence of the spin and orbital poles, which is both observed and expected on the basis of tidal evolution, the changes in orbital plane orientation are small. The maximum excursion in orbital orientation due to the oblateness of the primary is twice the angular separation between spin and orbital poles, which is driven to zero by tides (*18*).

The nonzero J_2 results in an advance of the line of apsides at a rate $d\omega/dt \cong -2d\Omega/dt$. This affects the determination of the orbital period, because the observed mean motion is not identical to the Keplerian mean motion; i.e., that which would be observed for an orbit around an idealized (spherical, homogeneous) primary of the same mass (*19*). Because the axial ratios, mass distribution, and therefore J_2 are poorly known, we feel that the Keplerian orbital period is not known to better than 1 part in $3J_2 (R/a)^2$ (~1%; i.e., $P = 3.596 \pm 0.04$ days). The Keplerian and observed values of a also differ as a result of the primary oblateness. The relative uncertainty that we adopt for a is three times the formal uncertainty or ~2%; i.e., $a = 1063 \pm 23$ km. With those error bars on P and a, the relative uncertainty on our mass determination is ~6%. Our density measurement and uncertainties remain unchanged at 2.37 ± 0.4 g cm^{-3}, because the error bars are largely dominated by uncertainties in the size of the primary.

With the lightcurve-derived primary spin period of ~4.15 hours (*20*), one can show

Table 1. Positions of the secondary with respect to the primary, and postfit residuals. The epochs of observations are given as modified Julian dates (MJD), the separations between primary and secondary are given in arc seconds (″), and the position angles (PA) of the secondary with respect to the primary are given in degrees. Postfit residuals (observed minus computed) are normalized to the measurement uncertainties.

Epoch (MJD)	Sep. (″)	PA(°)	$(O_x - C_x)/\sigma_x$	$(O_y - C_y)/\sigma_y$	Detector
52150.615	0.480	157.5	0.057	1.002	SCAM
52152.606	0.566	348.7	−0.042	0.921	SCAM
52153.570	0.245	72.9	−0.345	0.303	SCAM
52159.522	0.503	333.4	−1.205	0.448	PHARO
52160.508	0.335	31.6	−0.054	−0.658	PHARO
52161.457	0.546	164.1	−0.087	−0.176	PHARO
52253.261	0.887	350.2	0.451	−0.053	SCAM
52637.592	0.522	75.5	−0.704	−0.626	NIRC2
52637.678	0.538	66.4	0.585	0.567	NIRC2

Table 2. Best-fit ($\chi^2 = 0.5$) parameter estimates, their formal errors, and correlation matrix. The orbital parameters are period P, semi-major axis a, epoch of pericenter passage T, longitude of perihelion Ω, and inclination i. The argument of pericenter is zero. The best-fit solution based on our first six observations alone yields parameters within 1% of those and a mass within 3% of our current best estimate, albeit with larger formal errors.

Parameter	Estimate	P	a	T	Ω	i
P (days)	3.59567 ± 0.0001	1.00				
a (km)	1063 ± 7.6	−0.20	1.00			
T (MJD)	52152.014 ± 0.01	−0.86	0.21	1.00		
Ω (°)	286.2 ± 1	0.32	−0.22	−0.25	1.00	
i (°)	93.4 ± 1	−0.24	−0.02	0.31	0.46	1.00

that the orbital angular momentum represents only a ~15% fraction of the primary spin angular momentum. Therefore, it is conceivable that the total angular momentum of the system was exclusively in the form of spin angular momentum before formation of the binary (*21*). The secondary may have formed close to the primary and gradually evolved outward due to tidal interactions. The primary loses spin angular momentum (the length of day increases) as the secondary gains orbital angular momentum (the orbit expands), just as in the Earth-Moon system. The time scale for orbital expansion depends linearly on Q_p, the tidal dissipation factor (number of cycles to damp), and inversely on k_{2p}, the response coefficient to a centrifugal potential. The subscript p indicates quantities related to the primary, because the relevant tides are those raised by the secondary on the primary. For relatively small bodies like Kalliope and its companion, k_{2p} is largely dictated by elastic forces rather than gravitational forces, and hence k_{2p} is inversely proportional to the rigidity or shear modulus μ_p. Tidal evolution scenarios allow us to place useful constraints on asteroid material properties. If the secondary formed close to the primary ~4.6 billion years ago, one can use the standard tidal evolution formula (*17*) to constrain $k_{2p}/Q_p \cong 4 \times 10^{-7}$. For $Q = 100$, typical of silicate-rich bodies (*22*), one finds a rigidity $\mu_p \cong 5 \times 10^{10}$ Pa, in agreement with values expected for rock under overburden pressures from 0 to ~10 MPa (*23*). The pressure at the center of Kalliope is ~6.4 MPa.

The evolution of the eccentricity is a competing process between tides raised on the primary, which tend to raise the eccentricity, and tides raised on the secondary, which tend to decrease the eccentricity (*24*):

$$\frac{de}{dt} = \frac{57}{8}\frac{k_{2p}}{Q_p}\frac{M_s}{M_p}\left(\frac{R_p}{a}\right)^5 ne - \frac{21}{2}\frac{k_{2s}}{Q_s}\frac{M_p}{M_s}\left(\frac{R_s}{a}\right)^5 ne \quad (2)$$

Using the inverse dependence of the k_2 Love number on rigidity, the condition for eccentricity damping becomes

$$\frac{19}{28}\frac{R_p}{R_s}\frac{\mu_s}{\mu_p}\frac{Q_s}{Q_p} < 1 \quad (3)$$

This is an interesting constraint because it allows us to compare the mechanical properties of the primary and secondary, especially if we find that most main-belt asteroid satellites are on circular orbits, and especially for systems with large R_p/R_s ratios. Because self-gravity is negligible compared to elasticity in the tidal response of these bodies, one does not expect a dependence of Q on size (*24*). However, the Q of the two components may be different if they are structurally different. For instance, a gravitationally bound aggregate may undergo considerable friction between individual fragments and therefore have a low Q. There is also evidence that elastic moduli decrease as a function of damage in fragmented or shock-damaged rocks (*25*). The fact that the orbit is circular implies that μQ is smaller for the secondary than for the primary, and that tidal dissipation is more effective in the secondary than in the primary. This suggests that the secondary may be a gravitationally bound aggregate formed by the reaccumulation of impact ejecta after a collision on the primary.

Kaula (*26*) showed that inclination damping occurs as the orbit expands as a result of tides raised by the secondary on the primary. Because the rate of orbital expansion is proportional to the $-(11/2)$ power of a, the evolution of a and i was most rapid early on. The binary has been asymptotically approaching the end-state of tidal evolution, where the system is fully despun (doubly synchronous similar to Pluto-Charon) with a secondary orbiting in the equatorial plane of the primary. The alignment of the spin and orbital poles, within observational uncertainties, is therefore not surprising. The fact that the satellite orbits in the same sense of rotation as that of the spin of Kalliope places additional constraints on possible formation scenarios. There would be no preference for the sense of rotation in the case of gravitational capture of two fragments following a fully disruptive collision. But impact ejecta reaccumulating into a satellite after a subcatastrophic collision may preferentially adopt an orbit in the same sense of rotation as that of the surviving primary.

It is fruitful to compare the orbital evolution time scale to that required for the secondary to reach spin-lock, where the spin and orbital periods are identical. The ratio depends on material properties exactly as in (*3*), which is less than unity given that $e = 0$. We find that the time scale for spin-lock is an order of magnitude less than the orbital evolution time scale, regardless of the formation age of the system; hence, we expect the secondary to be synchronously rotating. Satellites with rotation periods that have been synchronized by tidal forces are expected to reach a Cassini state. The synchronous rotation state may be evident in radar or lightcurve data. With a flux that is ~25 less than that of the primary, the secondary is not expected to have affected the lightcurve analysis, but its rotation period may nevertheless appear as a faint modulation to the lightcurve.

The density of the primary (2.37 ± 0.4 g cm^{-3}) is about a third that of the most commonly accepted meteorite analogs (*27*). Because iron meteorites have almost zero microporosity and a grain density of 7.4 g cm^{-3} (*28*), reconciling these two densities would imply a macroporosity of $68 \pm 5\%$. We find it unlikely that the remnant core of a differentiated object can sustain a volume of void space that is twice the volume of material. For instance, the least efficient packing of uniformly sized spheres yields a porosity of only 48%. The highest porosity reported for an asteroid with accurate size/mass determination is ~50% for 253 Mathilde (*29*), although few asteroid porosities are known (*28*, *30*). It would take a 3σ error in the IRAS size determination (*14*) to make our density measurement compatible with a disrupted metal core with 50% porosity, which we also consider unlikely (*31*). Therefore, we conclude that Kalliope, an M-type asteroid, is not predominantly composed of metal and is not a progenitor of iron meteorites. (That the asteroid would be composed of a low-density mantle and high-density metallic crust is also extremely unlikely.) If Kalliope were instead an undifferentiated body composed of chondritic material (grain density of ~3.5 g cm^{-3}), the required porosity would be ~30%, typical of fractured or even loosely consolidated asteroids (*28*).

A chondritic composition would be more consistent with recent inferences based on spectroscopic data (*32*, *33*). Ten out of 27 M-type asteroids observed by Rivkin *et al.* (*32*), including Kalliope, are reported to have an absorption feature at 3 μm that the authors interpret as diagnostic of water of hydration. This finding appears to contradict the iron core hypothesis because hydrated minerals would not survive the elevated temperatures required for differentiation. However, explaining water of hydration on the parent bodies of enstatite chondrites that formed in a reducing environment is not entirely straightforward either. Hardersen *et al.* (*33*) report the detection of a weak 0.9-μm feature on at least 4 M-type asteroids, which they interpret as diagnostic of orthopyroxene, also indicative of a reducing environment. The spectroscopic data therefore do not provide a unique fit to any particular mineralogic composition (*34*). Radar observations provide an obvious way to distinguish metal-rich objects (*35*). The radar data indicate that some M-type asteroids are largely metallic whereas others are largely rock (*36*), consistent with the dichotomy observed by Rivkin *et al.* (*32*). Kalliope has a radar cross section that is typical of a stony object (*37*).

References and Notes

1. J. Gradie, E. Tedesco, *Science* **216**, 1405 (1982).
2. S. J. Bus, F. Vilas, M. A. Barucci, *Asteroids III*, W. F. Bottke, A. Cellino, P. Paolicchi, R. Binzel, Eds. (Univ. of Arizona Press, Tucson, AZ, 2002), pp. 169–182.
3. The M type is one of the most common asteroid spectral types after the C types (flat spectra suggestive of carbon-rich material) and S types (red spectra with absorption features indicative of silicates).
4. M. J. Gaffey, *J. Geophys. Res.* **81**, 905 (1976).
5. E. A. Cloutis, M. J. Gaffey, D. G. W. Smith, R. S. J. Lambert, *J. Geophys. Res.* **95**, 281 (1990).
6. J. L. Margot, M. E. Brown, *IAU Circ.* **7703** (2001).
7. The observations are part of a systematic survey to search for and characterize binary systems in the main belt of asteroids. An important goal is to compare the

binary systems in the near-Earth, main-belt, and Kuiper-belt populations, because they provide a wealth of information about physical properties, formation processes, and collisional environments (*38*–*40*).
8. Kalliope was named for the Muse of heroic poetry (*41*). The authors propose that the companion be named Linus, who in various Greek mythological accounts is portrayed as the son of Kalliope and the inventor of melody and rhythm.
9. P. L. Wizinowich *et al.*, *Proc. SPIE* **4007**, 2 (2000).
10. I. S. McLean *et al.*, *Proc. SPIE* **3354**, 566 (1998).
11. T. L. Hayward *et al.*, *Publ. Astron. Soc. Pac.* **113**, 105 (2001).
12. J. L. Margot *et al.*, *Science* **296**, 1445 (2002).
13. The software has been thoroughly validated with a wide range of binary systems, including near-Earth and main-belt asteroids, the Pluto-Charon system (*42*), the 1998 WW31 KBO binary (*43*), and binary stars (*44*).
14. E. F. Tedesco, P. V. Noah, M. Noah, S. D. Price, *Astron. J.* **123**, 1056 (2002).
15. P. Magnusson *et al.*, *Asteroids, Comets, Meteors 1993* (1994), pp. 471–476.
16. P. Magnusson, *Icarus* **85**, 229 (1990).
17. C. D. Murray, S. F. Dermott, *Solar System Dynamics* (Cambridge Univ. Press, 1999).
18. The time scales for orbital plane precession due to the influence of the Sun and Jupiter are on the order of 2500 years and can be neglected.
19. R. Greenberg, *Astron. J.* **86**, 912 (1981).
20. C.-I. Lagerkvist, A. Claesson, *Earth Moon Planets* **72**, 219 (1996).
21. This is unlike some binary Kuiper belt objects that have so much angular momentum that formation by breakup of a single body is not conceivable (*38*). The amount of orbital angular momentum in the Kalliope system is not sufficient to invoke formation by spin-up of the primary beyond the breakup rate and mass shedding, as in the case of near-Earth asteroid binaries (*12*).
22. P. Goldreich, S. Soter, *Icarus* **5**, 375 (1966).
23. A. M. Dziewonski, D. L. Anderson, *Phys. Earth Planet. Int.* **25**, 297 (1981).
24. P. Goldreich, *Mon. Not. R. Astron. Soc.* **126**, 257 (1963).
25. H. He, T. J. Ahrens, *Int. J. Rock Mech. Min. Sci. Geomech.* **31**, 525 (1994).
26. W. M. Kaula, *Rev. Geophys.* **2**, 661 (1964).
27. Using data from a 1937 encounter between 16 Psyche and 94 Aurora, Viateau (*45*) finds that M-type Psyche also has a low density, although the author indicates that there may be biases in the mass determination.
28. D. T. Britt, D. Yeomans, K. Housen, G. Consolmagno, *Asteroids III*, W. F. Bottke, A. Cellino, P. Paolicchi, R. Binzel, Eds. (Univ. of Arizona Press, Tucson, AZ, 2002), pp. 485–500.
29. D. K. Yeomans *et al.*, *Science* **278**, 2106 (1997).
30. J. L. Hilton, *Asteroids III*, W. F. Bottke, A. Cellino, P. Paolicchi, R. Binzel, Eds. (Univ. of Arizona Press, Tucson, AZ, 2002), pp. 103–112.
31. There are independent measurements of the size of Kalliope. E. Bowell, T. Gehrels, and B. Zellner (*46*) obtain a diameter of 175 km with the highest quality code, which gives a density that is 10% higher than the result based on the IRAS value, and a porosity of 65% if one assumes a metallic composition.
32. A. S. Rivkin, E. S. Howell, L. A. Lebofsky, B. E. Clark, D. T. Britt, *Icarus* **145**, 351 (2000).
33. P. S. Hardersen, M. J. Gaffey, P. A. Abell, *Lunar Planet. Inst. Conf. Abstr.* **33**, 1148 (2002).
34. M. J. Gaffey, E. A. Cloutis, M. S. Kelley, K. L. Reed, *Asteroids III*, W. F. Bottke, A. Cellino, P. Paolicchi, R. Binzel, Eds. (Univ. of Arizona Press, Tucson, AZ, 2002), pp. 183–204.
35. S. J. Ostro *et al.*, *Science* **252**, 1399 (1991).
36. C. Magri, G. J. Consolmagno, S. J. Ostro, L. A. M. Benner, B. R. Beeney, *Meteorit. Planet. Sci.* **36**, 1697 (2001).
37. C. Magri, M. C. Nolan, personal communication.
38. J. L. Margot, *Nature* **416**, 694 (2002).
39. J. A. Burns, *Science* **297**, 942 (2002).
40. W. J. Merline *et al.*, *Asteroids III*, W. F. Bottke, A. Cellino, P. Paolicchi, R. Binzel, Eds. (Univ. of Arizona Press, Tucson, AZ, 2002), pp. 289–312.
41. L. D. Schmadel, *Dictionary of Minor Planet Names* (Springer, Berlin, ed. 4, 1999).
42. D. J. Tholen, M. W. Buie, *Icarus* **125**, 245 (1997).
43. C. Veillet *et al.*, *Nature* **416**, 711 (2002).
44. W. D. Heintz, *Astrophys. J. Suppl.* **117**, 587 (1998).
45. B. Viateau, *Astron. Astrophys.* **354**, 725 (2000).
46. E. Bowell, T. Gehrels, B. Zellner, *Asteroids*, T. Gehrels, Ed. (Univ. of Arizona Press, Tucson, AZ, 1979), pp. 1108–1129.
47. We are grateful to M. Britton for follow-up observations at Palomar and to P. Goldreich, T. Ahrens, and M. Pritchard for insightful discussions. J.L.M. thanks S. Kulkarni for financial support. Some of the data presented here were obtained at the W. M. Keck Observatory, which is operated as a scientific partnership among the California Institute of Technology, the University of California, and the National Aeronautics and Space Administration. The observatory was made possible by the generous financial support of the W. M. Keck Foundation. We extend special thanks to those of Hawaiian ancestry on whose sacred mountain we are privileged to be guests. Without their generous hospitality, many of the observations presented here would not have been possible.

17 April 2003; accepted 19 May 2003

Episodic Tremor and Slip on the Cascadia Subduction Zone: The Chatter of Silent Slip

Garry Rogers* and Herb Dragert

We found that repeated slow slip events observed on the deeper interface of the northern Cascadia subduction zone, which were at first thought to be silent, have unique nonearthquake seismic signatures. Tremorlike seismic signals were found to correlate temporally and spatially with slip events identified from crustal motion data spanning the past 6 years. During the period between slips, tremor activity is minor or nonexistent. We call this associated tremor and slip phenomenon episodic tremor and slip (ETS) and propose that ETS activity can be used as a real-time indicator of stress loading of the Cascadia megathrust earthquake zone.

The Cascadia subduction zone is a region that has repeatedly ruptured in great thrust earthquakes of moment magnitude greater than 8 (*1*, *2*). Recently, slip events have been detected on the deeper (25- to 45-km) part of the northern Cascadia subduction zone interface by observation of transient surface deformation on a network of continuously recording Global Positioning System (GPS) sites (*3*). The slip events occur down-dip from the currently locked, seismogenic portion of the subduction zone (*4*), and, for the geographic region around Victoria, British Columbia, (Fig. 1), repeat at 13- to 16-month intervals (*5*). These slips were not accompanied by earthquakes and were thought to be seismically silent. However, unique nonearthquake signals that accompany the occurrence of slip have been identified using data from the regional digital seismic network. These pulsating, tremorlike seismic signals are similar to those reported in the forearc region of Japan (*6*, *7*), but the signals observed in Cascadia correlate temporally and spatially with six deep slip events that have occurred over the past 7 years. At other times, this tremor activity is minor or nonexistent. These tremors have a lower frequency content than nearby earthquakes, and they are uncorrelated with the deep or shallow earthquake patterns in the region. They have been observed only in the subduction zone region and specifically in the same region as the deep slip events. We refer to this associated tremor and slip phenomenon as episodic tremor and slip (ETS).

The seismic tremors described here are different from small earthquakes. The frequency content is mainly between 1 and 5 Hz, whereas most of the energy in small earthquakes is above 10 Hz. A tremor onset is usually emergent and the signal consists of pulses of energy, often about a minute in duration. A continuous signal may last from a few minutes to several days. Tremors are strongest on horizontal seismographs and move across the seismic network at shear wave velocities. A tremor on an individual seismograph is unremarkable and does not appear different from transient noise due to wind or cultural sources. It is only when a number of seismograph signals are viewed together that the similarity in the envelope of the seismic signal at each site identifies the signal as ETS (Fig. 1).

The tremor activity migrates along the strike of the subduction zone in conjunction with the deep slip events at rates ranging from about 5 to 15 km per day. Sometimes there is a gradual migration, but at other times there is a sudden jump from one region of the subduction fault to another. Tremors vary in amplitude, and the strongest can be detected as far as 300 km from the source region. During an ETS event, tremor activity lasts about 10 to 20 days in any one region and contains tremor sequences with amplitudes that are at least a factor of 10 larger

Geological Survey of Canada, Pacific Geoscience Centre, 9860 West Saanich Road, Sidney, British Columbia, Canada V8L 4B2.

*To whom correspondence should be addressed. E-mail: rogers@pgc.nrcan.gc.ca